PFG – Journal of Photogrammetry, Remote Sensing and Geoinformation Science
https://doi.org/10.1007/s41064-024-00330-x

ORIGINAL ARTICLE

Ground Resolved Distance Estimation of Sentinel-2 Imagery Using Edge-based Scene-Driven Approach

Farzaneh Dadrass Javan[1] · Farhad Samadzadegan[2] · Ahmad Toosi[2] · Mathias Schneider[3] · Claudio Persello[1]

Received: 17 June 2024 / Accepted: 4 December 2024

Abstract
Sentinel-2 satellite provides freely accessible multispectral images used in various remote sensing (RS) applications, where spatial resolution is crucial. The Ground Sampling Distance (GSD) for Sentinel's visible and near-infrared (VNIR) bands is specified at 10 meters, but it may not accurately reflect ground resolution due to environmental effects. As a result, Ground Resolved Distance (GRD) serves as an alternative measure for actual resolution, but information about Sentinel GRD is lacking, calibration targets are not always available, and GRD may vary across different tiles. This paper estimates Sentinel's GRD using a scene-driven approach that analyzes the edges of natural targets, reducing the challenges associated with artificial targets. The method involves selecting suitable natural targets based on their geometric and spectral characteristics, sub-pixel edge extraction, estimating the Edge Spread Function (ESF), generating the Line Spread Function (LSF), and calculating the Full-width at Half Maximum (FWHM). Two tiles of Sentinel-2 imagery from the Shadnagar Calibration Facility, India, and Baotou, China, were analyzed. The analysis of 40 natural targets revealed average GRD values of 12.65 m, 12.40 m, 12.49 m, and 12.58 m for the red, green, blue, and NIR bands, respectively, aligning closely with results from calibration targets. The method demonstrated high accuracy and precision with a total RMSE of approximately 0.77 m and a total standard deviation of 0.19 m, respectively.

Keywords Earth observation · Satellite imagery · Sentinel-2 · European Space Agency (ESA) · Ground sampling distance (GSD) · Ground resolved distance (GRD)

1 Introduction

Earth observation satellites use remote sensing (RS) technology to capture geospatial imagery of Earth. The Sentinel-2A and Sentinel-2B twin optical imaging satellites, operated by the European Space Agency (ESA), provide rich spectral information in visible and invisible parts of the electromagnetic (EM) spectrum and high temporal resolution. These satellites operate as 13 spectral bands free of charge. The spatial resolution varies for different spectral bands. The visible (red, green, and blue bands) and near-infrared (NIR) bands, collectively known as VNIR bands, offer a resolution of 10 meters (m). The resolution for other invisible bands is 20–60 m (Drusch et al. 2012).

Various parameters define an RS imaging system, including spatial, spectral, temporal, and radiometric resolutions (Joseph 2005). The assessment of spatial resolution in satellite imagery has been a topic of regular research since the emergence of RS imagers (Choi et al. 2019; Crespi and De Vendictis 2009; NASA 1973; Stankevich 2020; Thomson 2009; Townshend 1981; Valenzuela et al. 2022; Valenzuela and Reyes 2019; Wang and Li 1999). Spatial resolution is commonly quantified using the Ground Sampling Distance (GSD), representing the distance between adjacent pixels on the ground (Lee and Sull 2019; Pampanoni et al. 2024; Valenzuela et al. 2022). GSD is defined during sensor design and relies on the RS imaging geometry (Pampanoni et al. 2024; Valenzuela et al. 2022). Essentially, it is based on a mathematical formulation and is easily calculated using a formula (Sun et al. 2021). Therefore, it offers the nominal spatial resolution of an RS system under ideal con-

✉ Farzaneh Dadrass Javan
f.dadrassjavan@utwente.nl

[1] Faculty of Geo-Information Science and Earth Observation (ITC), University of Twente, Enschede, The Netherlands

[2] School of Surveying and Geospatial Engineering, University College of Engineering, University of Tehran, Tehran, Iran

[3] Institut für Methodik der Fernerkundung (IMF), Deutsches Zentrum für Luft- und Raumfahrt (DLR), 82234 Weßling, Germany

Published online: 16 January 2025

ditions (Cramer et al. 2020; Meißner et al. 2019; Topan et al. 2005), failing to consider the realities of data acquisition. Due to environmental factors, GSD inadequately represents the actual ground resolving power of an RS imaging system (Crespi and De Vendictis 2009; Kim et al. 2008).

Ground Resolved Distance (GRD) estimates the smallest feature size reliably resolvable by an imaging system (Campbell and Wynne 2011). Unlike GSD, GRD considers environmental conditions such as lighting, atmospheric particles, humidity, and air density (Kubišta and Surový 2021; Topan et al. 2005). GRD differs from GSD; ideally, their ratio approaches 1 in optimal conditions. This ratio is sometimes employed as an indicator to assess relative image sharpness (Lim et al. 2018a). While the sensor's nominal GSD provides a theoretical measure, true resolving power is assessed under actual imaging conditions using calibration targets and image analysis methods, such as ambiguity circle or edge response analysis.

In various applications of Sentinel-2 imagery, such as mapping, semantic segmentation, sub-pixel landscape feature detection, and object analysis (Belgiu and Csillik 2018; Clabaut et al. 2024; Lasko et al. 2024; Li et al. 2024; Liu et al. 2024; Mifdal et al. 2021; Nguyen et al. 2022; Radoux et al. 2016; Saleem and Awange 2019; Samadzadegan et al. 2023; Toosi et al. 2022; Wu et al. 2024; Xu et al. 2024; Zhao et al. 2019), the VNIR bands, with a GSD of 10 m, are critical to the dataset, surpassing the importance of other bands, which have GSDs of 20 to 60 m. However, as with any RS system, the ground resolution of Sentinel-2 bands often deviates from the nominal GSD values. Therefore, estimating the GRD for Sentinel-2 imagery is necessary.

The primary approach for assessing GRD in RS imagery involves using resolution calibration targets (Bushahab et al. 2014; Choi et al. 2019). These targets are predetermined patterns printed on banners or painted on the ground (Li et al. 2015). Orych (2015) provides an overview of state-of-the-art targets. The imaging system captures these targets, and subsequent analysis estimates the GRD (Kubišta and Surový 2021; Lim et al. 2018a; Lim et al. 2018b). However, creating large targets is challenging, making them suitable only for high-resolution satellite and aerial imagery. Thus, they are less used for medium-resolution satellites like Sentinel and Landsat.

An alternative approach for estimating GRD involves utilizing natural targets (Kim et al. 2010a; Kim and Kim 2011b; Li et al. 2014). Natural targets include structures like building roofs (Javan et al. 2013; Kim and Kim 2011a), particularly large industrial buildings, extensive roadways, and boundaries between adjacent lands (Cenci et al. 2021; Li et al. 2014; Pampanoni et al. 2020; Pampanoni et al. 2022; Pampanoni et al. 2024). These targets should have straight, sharp edges and color or spectral characteristics similar to artificial targets (Javan et al. 2013). The objects must be large enough to be easily discernible and appropriate for resolution evaluation relative to the pixel size. Examples include LUECKE farms[1] (Robinson et al. 2004).

This paper introduces a semi-automatic edge-based scene-driven approach to estimate Sentinel GRD for the first time. This method addresses the impracticality of creating large artificial targets for every Sentinel tile. The paper's contribution is twofold: it determines the true spatial resolution of Sentinel imagery and explores the accuracy and precision of resolution estimation using natural targets—an approach previously unexplored for middle-resolution satellite imagery.

2 Related Works

Research on ground resolution assessment uses either artificial targets for airborne and spaceborne imagery, or natural features.

2.1 Literature on Spatial Resolution Estimation of RS Imageries Using Calibration Targets

Image spatial quality and resolvability assessment in the field of RS and photogrammetry often rely on specially manufactured artificial targets. These targets serve calibration, validation, and field testing purposes (Salamonowicz 1982; Schott et al. 2012). This requires specific arrangements such as target size and orientation (Kim and Kim 2011b).

Topan et al. (2005) investigated and highlighted the distinction between the nominal GSD and the effective or true GSD (tGSD) (Cramer et al. 2020; Meißner et al. 2019), also known as GRD. They highlighted the impact of factors, including optics, and atmosphere, on the GRD of images. According to their findings, the effective GSD differs from the nominal value and can be evaluated through edge analysis. Meißner et al. (2019) examined tGSD by comparing methods for determining resolution using artificial targets. They compared bar test charts, slanted-edge targets, and Siemens-Star targets. Additionally, they evaluated the Slanted-Edge and Siemens-Star methods with ideal images convolved using known parameters, demonstrating the reliability of both techniques. Their evaluation method was based on the measurement of model-based Modulation Transfer Function (MTF) and Point Spread Function (PSF). Choi et al. (2019) applied edge analysis in satellite image fusion, employing edge targets. They manually cropped portions of the targets and extracted the edges. Addition-

[1] A forest was selectively cleared to spell the landowner's name "LUECKE" with the remaining trees. This feature is used for evaluating the resolution of astronaut photographs.

ally, they estimated the signal-to-noise ratio (SNR) and the Nyquist value of the MTF based on both the Edge Spread Function (ESF) and the Line Spread Function (LSF). Tao and Muller (2021) in research aiming at super-resolution restoration of space-borne images used different types of artificial targets for resolution evaluation of images. They assessed their method by zooming in on the edges of the targets to visually determine which super-resolution technique performed better. Additionally, they compared the results with the slanted-edge profile measurements.

Scott et al. (2024) developed a Multi-Edge Slant Target for unlocalized MTF measurement of airborne RS system payloads. Their approach experimentally characterizes the MTF of airborne assemblies in a laboratory environment. Dubey et al. (2024) highlight oversights and errors in MTF estimation using the slant-edge technique for high-resolution satellite sensors. They focus on optimal edge width estimation and empirical modeling of the slant edge.

UAV-based RS images offer superior GSD and GRD compared to satellites and manned aircraft due to lower operational altitudes (Lim et al. 2018a), prompting researchers to evaluate UAV image resolution using artificial targets (Conran 2024). Dąbrowski and Jenerowicz (2015) and Dabrowski et al. (2015) developed the Portable Imagery Quality Assessment Test Field (PIQuAT) for assessing image quality and resolution from UAV sensors. The PIQuAT evaluates spatial, spectral, and radiometric resolution.

Lim et al. (2018a) employed an edge-based method to derive image quality parameters, including Relative Edge Response (RER), SNR, MTF, GRD, and National Imagery Interpretability Rating Scale (NIIRS) (Leachtenauer et al. 1997). The results showed that changes in imaging altitude impacted GSD and NIIRS, while GRD and image sharpness were optimal at certain altitudes. The researchers extracted edge details, providing measures to assess image resolution. The process involved estimating the ESF through edge analysis, differentiating it to obtain the LSF, and performing a Fourier transform on the LSF to calculate the MTF. Lim et al. (2018b) extracted GRD by analyzing the edge calibration target at various altitudes. They used GRD and the GRD-to-GSD ratio to evaluate image sharpness.

Cramer et al. (2020) emphasized the significance of considering the concepts of GRD in assessing the quality of UAV images. Siemens targets were employed as part of their testing framework. Kubišta and Surový (2021) identified the relationship between resolution and acquisition conditions. They tested different heights, flight speeds, and light conditions for their impact on GRD. Height was the most significant factor, followed by speed, while light conditions had the least influence. Ghassoun et al. (2021) discussed image quality, spatial resolution, and GRD in UAV photogrammetry. They noted that a camera's resolving power depends on criteria like the standard deviation of the PSF, reflecting image space and comparing performance, or its Full Width at Half Maximum (FWHM).

2.2 Literature on Spatial Resolution Estimation of RS Imageries Using Natural Targets

Several scholars have conducted edge analysis of natural targets to estimate GRD and NIIRS values. Kim et al. (2008) proposed a method for estimating and validating NIIRS through image-based techniques, specifically tailored for high-resolution satellite imageries. In their study, the selection of natural target edges. Kim et al. (2010b) conducted NIIRS estimation using edge analysis of natural targets. The edges for their evaluation were extracted both manually and automatically, and the analysis was performed on ESFs and PSFs. Kim et al. (2010a) developed a method for measuring GRD utilizing natural targets. They extracted edge points from both artificial and natural targets and analyzed the parameters associated with the ESF and LSF. Kim and Kim (2011a) and Kim and Kim (2011b) emphasized the need for automated GRD and NIIRS estimation in high-resolution satellite imagery through edge profile analysis of natural targets. They developed a natural target-based method for estimating NIIRS, reducing dependency on artificial targets. Their evaluation method was based on semi-automatic edge profile extraction and ESF. However, the selection of edges in shadowed regions, building roofs, field boundaries, and boundaries between land and water areas, had insufficient contrast. This lack of contrast caused issues in generating ESFs and subsequently in GRD evaluation.

Javan et al. (2013) proposed a method for assessing the spatial quality of pan-sharpened high-resolution satellite imagery. Their method involved an automated estimation of an edge-based metric, focusing on the assessment of natural targets. Li et al. (2014) evaluated the ZY-3 panchromatic band using the General Image Quality Equation (GIQE) (Leachtenauer et al. 1997). Their method for resolution evaluation and NIIRS prediction was based on the analysis of edges between adjacent land areas. Mhangara et al. (2020) assessed the interpretability of the nSight-1 nanosatellite, capturing images at 30–32 m resolution, using Landsat-8 as a reference. They evaluated image quality with the Blind/Referenceless Image Spatial Quality Evaluator (BRISQUE) and quantified interpretability using NIIRS.

Cenci et al. (2021) introduced a semi-automatic approach to evaluate the sharpness of optical imagery using natural targets' edges. They focused on Landsat-8 data and demonstrated that their method is capable of reliably assessing the sharpness of the image. Pampanoni et al. (2020, 2022, 2024) developed an automatic method for sharpness assessment and spatial resolution determination of satellite imagery. Their research encompassed various types of im-

agery with different spatial and spectral resolutions. Their method identified different natural targets using analysis of DN values. Their meta-analysis reported parameters indicating spatial resolution and sharpness, illustrating their relationship with the SNR of the image.

In summarizing the literature reviewed, it is evident that while much attention has been given to ground resolution assessment using calibration targets, research with natural targets has focused on UAV images or high/very high-resolution satellite imagery. There has been a lack of studies evaluating GRD of middle-resolution satellite imagery such as Sentinel-2. The absence of artificial calibration targets covering Sentinel tiles worldwide (which is practically infeasible to achieve for every Sentinel imaging area), combined with the considerable cost and effort required to create such large targets, makes RS researchers explore natural targets as substitutes for resolution assessment.

Despite interest in using natural targets, the reliability of spatial resolution assessments particularly for medium-resolution satellite imagery remains unverified. Testing the applicability of natural target-based methods for resolution evaluation of RS imagery needs investigation. Specifically, the accuracy (validated against reference artificial calibration targets) and precision (consistency across different natural targets) of these methods require examination.

Given that GSD may not accurately reflect the spatial resolving power of Sentinel Multispectral Instrument (MSI) and with the growing emphasis on spatial resolution assessment in satellite imagery (Cenci et al. 2021; Choi et al. 2019; Pampanoni et al. 2020; Pampanoni et al. 2022; Pampanoni et al. 2024), there is a need for more efficient criteria to determine the actual resolution of imagery. This is especially crucial for Sentinel-2 data, which, due to their open-access nature, have garnered significant attention.

Building on the aforementioned research and addressing the identified gap, our method employs a natural target-based approach to improve the accuracy and efficiency of spatial resolution assessment in RS imagery, while using artificial targets to verify the accuracy of the method. The novelty lies in two aspects: firstly, evaluating the effectiveness of natural targets in estimating the GRD of medium-resolution satellite imagery in terms of accuracy and precision (this is the first research to test whether natural targets provide accurate results comparable to those obtained from calibration targets, and to assess the precision of these results), and secondly, providing an estimation of GRD for

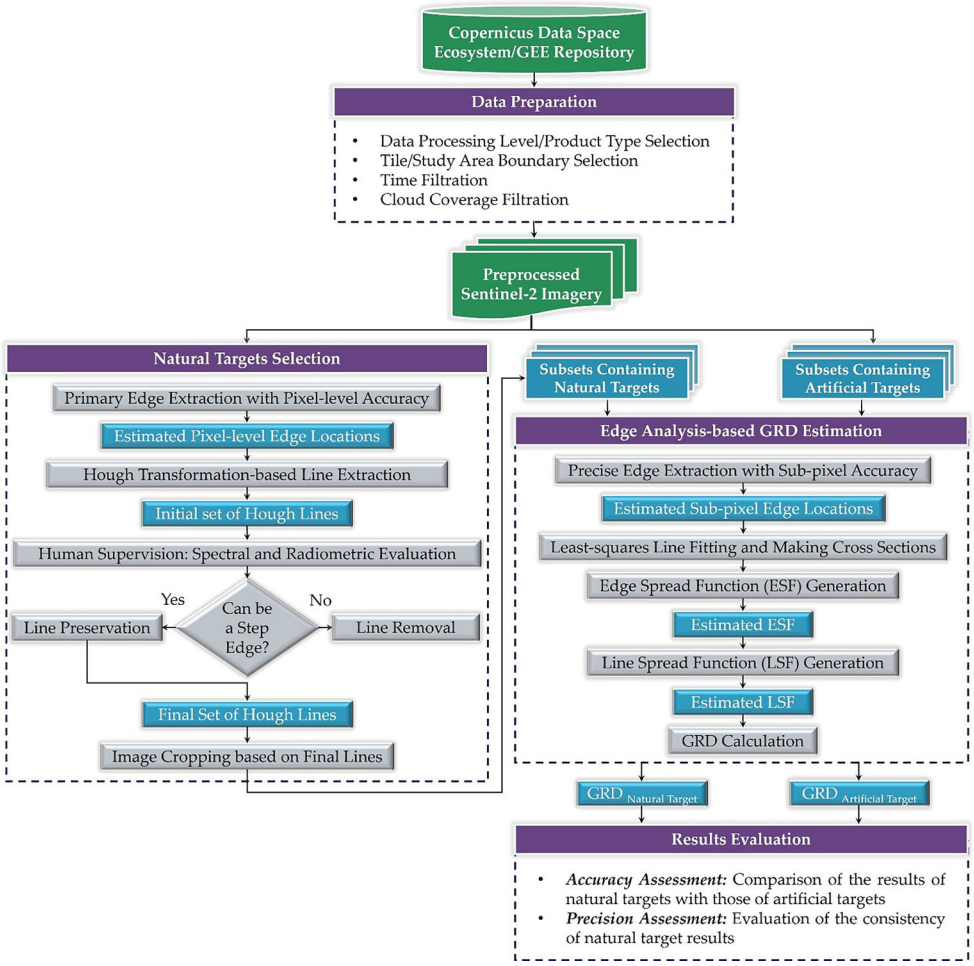

Fig. 1 Workflow of the proposed method for estimation of Sentinel-2 imagery GRD using natural targets

Sentinel-2 imagery for the first time. Due to the impracticality of creating a large number of artificial targets of appropriate size, and the limited availability of suitable edges in low- to medium-resolution images, the contribution of our paper regarding this type of satellite imagery would be of interest to the RS community.

3 Materials and Methods

This section describes the methodology to estimate the GRD of Sentinel-2 imagery. It also discusses the availability of large artificial targets globally and the dataset used.

3.1 Methodology

The methodology for estimating GRD in medium-resolution satellite imagery, specifically Sentinel-2 images, is shown in Fig. 1.

3.1.1 Data Preparation

In the initial step of the proposed method, known as the data preparation phase, a complete tile (granule) of Sentinel-2 imagery is retrieved from the Copernicus Data Space Ecosystem. The Sentinel-2 MSI sensor provides data in two processing levels: L2A (geometrically and atmospherically corrected, or surface reflectance) and L1C (top of atmosphere reflectance). For our purposes, we opt for the L2A surface reflectance data sourced from the data repositories. To minimize cloud coverage, the data are filtered based on the available filtration options. Furthermore, by setting the time range, data from the desired date are prepared.

3.1.2 Natural Targets Selection

The Sentinel tiles, which include artificial targets, are cropped to generate subsets that only contain the target area, with boundaries adjusted to fit the targets. A semi-automatic method is employed for natural targets intended to serve as resolution targets. Edge extraction is initially conducted using Canny (Canny 1986) to identify edge locations with pixel-level accuracy. The algorithm parameters are adjusted to ensure satisfactory edge extraction.

Subsequently, the Hough transformation (Duda and Hart 1972) is applied to the edge map to detect lines and extract line parameters. Algorithm parameters are adjusted based on the imagery's characteristics. Only the strongest lines are retained from the extracted lines by setting a threshold, while others are removed. The selection of the strongest lines uses a relative thresholding approach based on line length. Lines are sorted by length, and the top N_{top} longest are retained. This method keeps only the most prominent lines, likely representing significant edges for resolution estimation. The value of N_{top} is adjustable based on imagery characteristics and the desired balance between sensitivity and robustness in edge detection, allowing the approach to adapt to the relative strengths of detected lines in each image. Natural targets are required to exhibit characteristics similar to artificial targets: a straight line separating two areas, one dark (ideally black) and the other bright (ideally white), creating a step-edge behavior.

The extracted lines are also reviewed by human experts, and those where a square window containing them does not exhibit sufficient spectral contrast between the two sides of the Hough lines are deleted. In other words, we are searching for eligible edges[2] (see Cenci et al. 2021 for examples of eligible and non-eligible edges). Finally, a variety of candidate subsets are selected for use as natural targets. Due to the low resolution of Sentinel-2 imagery, developing a fully automatic algorithm for extracting image subsets is not straightforward, and therefore, is not pursued further.

3.1.3 Edge Analysis-based GRD Estimation

After acquiring subsets containing artificial and natural targets, the GRD estimation based on edge analysis involves five sub-steps: precise edge location estimation with sub-pixel accuracy, least-square line fitting and cross-section creation, ESF generation, LSF generation, and GRD calculation.

a) *Precise edge location estimation with sub-pixel accuracy:* The objective is to extract precise sub-pixel edge locations within subset images. The method employed here was proposed by Trujillo-Pino et al. (2013). The edge detection technique relies on an edge and acquisition model derived from the partial area effect, which avoids assuming continuity in image values. It achieves precise extraction of edge position, orientation, curvature, and contrast, in noisy images, blurred edges, low contrast areas, or closely situated contours. Given the common occurrence of these conditions in medium-resolution satellite imagery, this method is suitable for our purposes.

The sub-pixel edge extraction yields discrete edge pixel positions with sub-pixel accuracy. This output, rather than constituting a continuous edge or line, provides a collection of precise point locations. In the subsequent phase, these discrete points undergo a line fitting procedure, wherein

[2] Eligible edges are straight edges that exhibit a relatively step-like behavior and are contained within a window showing a suitable contrast between the dark and bright sides.

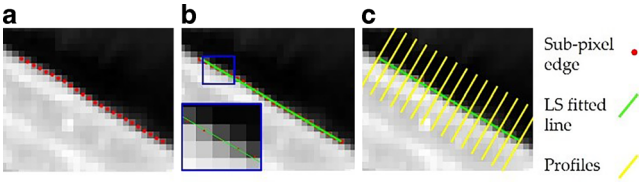

Fig. 2 Precise sub-pixel edge location extraction (**a**), least square line fitting (**b**) accompanied by profile generation (**c**)

a mathematical representation in the form of a linear equation is derived to approximate the edge.

b) *Least-square line fitting and cross sections (profiles) creation:* A least squares line fitting identifies the most suitable approximating line, minimizing the differences between the edge points on the approximating line and the provided edge point values. Randomly scattered residuals around zero indicate a good fit; however, if patterns are observed in the residuals, it may suggest that a linear fit is not appropriate for the data. A least squares adjustment derives the line parameters, namely slope (m) and intercept (c) (Eq. 1). The final edge location can be determined using the obtained line parameters. Fig. 2a depicts a sample of extracted edge locations, with the least squares line.

$$Y_{fit} = mX_{sub} + c \tag{1}$$

where (X_{sub}, Y_{fit}) is a set of edge locations, m represents the slope of the fitted line, and c is the y-intercept.

Due to the limitations of Eq. 1 in handling infinite slopes, we exclude vertical lines from our analysis. This exclusion strengthens our methodology and avoids potential computational problems. This limitation has little effect on our results, as the remaining non-vertical lines provide enough data for accurate resolution estimation.

It is important to distinguish between "edges" and "lines". Edges refer to pixels where significant changes in digital number (DN) values occur. These edges may manifest in various shapes, including straight or curved configurations. Conversely, lines denote straight linear features generated by fitting a linear model to edge pixels that exhibit a linear arrangement.

It is important to note that no specific threshold has been applied to the length of the fitted lines. As mentioned earlier, we select the top N_{top} lines from candidate lines. It is recommended that the lines be long enough to cover at least five pixels, more or less, to ensure the reliability of subsequent steps.

Once the line has been fitted to the sub-pixel edge location, cross-sections are generated perpendicular to the lines (Cenci et al. 2021). Each fitted line is divided into N_{seg} equal segments along the x-axis, denoted as $X_{Sub\text{-}divide}$. The value of N_{seg} is determined by the number of pixels the fitted line crosses. For each segment i, the perpendicular slope (m′) and intercept (c′) to the fitted line at the corresponding ($X_{Sub\text{-}divide}$[i], $Y_{fit\text{-}divide}$[i]) point are computed. The perpendicular slope is determined by $m\prime = -\frac{1}{m}$, where m represents the slope of the fitted line. Thus, the perpendicular intercept is defined as Eq. 2.

$$c' = Y_{fit-divide}[i] - m' \cdot X_{Sub-divide}[i] \tag{2}$$

The length of the perpendicular profile is a fraction of the image width or a predefined size. Once these steps have been completed, a variety of profiles, each with a predefined number and equal length, is generated (Fig. 2b).

c) *ESF generation:* ESF represents the response of the imaging system to an edge source (Pampanoni et al. 2024). Before generating the ESF, grayscale image intensities are normalized to the range [0,1] by subtracting the minimum DN value from the pixel's DN value, and then dividing the result by the difference between the maximum and minimum DN values (Banik et al. 2009; Javan et al. 2013; Mäkiharju et al. 2013). This normalization ensures consistent processing across all images and allows for meaningful comparisons of the ESF across different images. For each profile obtained in the previous step, the intensity values along the profile are extracted[3] and stored in the ESF matrix. The matrix has dimensions $L \times N_p$, where L[4] is the number of pixels along the profile and N_p is the number of profiles. Each column in the ESF matrix represents the intensity values along one profile. The mean of the intensity values across all profiles is calculated, representing the average ESF with L mean values. The averaging process is conducted on a pixel-by-pixel basis. For instance, for the ith pixel, if the DN values across L profiles are DN_1, DN_2, … , DN_L, these values are averaged. This process is repeated for each pixel position along the profile.

To smooth the ESF curve and reduce noise, various functions can be fitted, such as Sigmoid, Fermi, and cubic splines, as shown in previous studies (Cenci et al. 2021; Crespi and De Vendictis 2009; Meißner et al. 2019).

[3] Using the initial pixel (located on the fitted line) and the profiles (which determine the directions to extend on both sides of the fitted line), the intensity values of pixels along the transect can be easily retrieved.

[4] The parameter L does not have a universally applicable constant value. Rather, it should be calibrated to ensure that the DN value variations on both sides of the edges are accurately modeled. The optimal value for L is determined through iterative testing. Based on previous studies, values from 6 to 8 have proven adequate, although slight deviations from this range may be necessary depending on image characteristics.

However, due to the low resolution of Sentinel-2 imagery and the limited number of pixels along the profiles, approximating the ESF may distort the MSI sensor's behavior. We avoid using Sigmoid approximation. Instead, we employ linear interpolation to add points between neighboring ESF points (see Algorithm 1).

d) *LSF generation:* Following the generation of the ESF, differentiation is conducted, as outlined in Eq. 3.

$$LSF\,(n) = \frac{d}{dn}\,[ESF\,(n)] = ESF\,(n) - ESF(n-1) \quad (3)$$

where $\frac{d}{dn}[.]$ represents the differentiation operation. This gives the LSF, which represents the response of the imaging system to a line source (Pampanoni et al. 2024).

For higher-resolution imagery, a Gaussian function can be used to smooth the LSF and reduce noise (Javan et al. 2013; Meißner et al. 2019). However, we use the original, linear-interpolated LSF to maintain its true behavior, as fitting a Gaussian distorts the limited points in the LSF and affects GRD accuracy.

Algorithm 1. **ESF point augmentation using linear interpolation**

Inputs:

ESF: Original ESF vector

NoP: Number of points to insert between neighboring points

Output:

ESF_{int}: Interpolated ESF vector

Initialize ESF_{int} with ESF [1]

$n \leftarrow 1$

While $n \leq$ length(ESF)-1 **do:**

P1 $\leftarrow$ ESF $[n]$

P2 $\leftarrow$ ESF $[n+1]$

Add P1 to ESF_{int}

Calculate Pts_{int} between P1 & P2

Add Pts_{int} to ESF_{int}

$n \leftarrow n+1$

Add ESF[length(ESF)] to ESF_{int}

End while

e) *GRD calculation:* The calculation of GRD relies on a parameter associated with the normalized LSF[5], known as the Full-Width at Half Maximum (FWHM) (Cenci et al. 2021). FWHM represents the horizontal distance between two points on the normalized LSF curve where

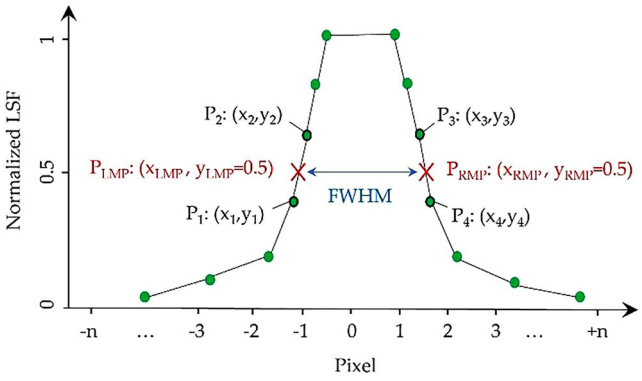

Fig. 3 FWHM estimation using linear interpolation technique

FWHM value indicates the difference between the abscissas at 0.5 (see Fig. 3). This metric shows the actual image resolution (Meißner et al. 2019). Smaller FWHM indicates steeper slopes of LSFs, which are associated with sharper images and higher resolution (Cenci et al. 2021).

To calculate the FWHM, typically employed when the LSF exhibits a Gaussian-like shape with a normal distribution, the value of $2\sqrt{2\ln 2}\sigma$ is utilized (Meißner et al. 2019). However, in the case of an LSF derived from medium-resolution Sentinel-2 imagery, we use the methodology of Crespi and De Vendictis (2009), as the LSF in this scenario lacks a continuous shape. As shown in Fig. 3, FWHM is the distance between the left mid-point (LMP) (Eq. 4) and right mid-point (RMP) (Eq. 5) identified through linear interpolation (Eq. 6).

$$x_{LMP} = (0.5 - y_2).\frac{x_1 - x_2}{y_1 - y_2} + x_2 \quad (4)$$

$$x_{RMP} = (0.5 - y_3).\frac{x_4 - x_3}{y_4 - y_3} + x_3 \quad (5)$$

$$FWHM = x_{RMP} - x_{LMP} \quad (6)$$

After obtaining the FWHM (in pixels), the GRD is determined by multiplying the FWHM by the GSD (Eq. 7).

$$GRD = FWHM \times Pixel\,Size = FWHM \times GSD \quad (7)$$

3.2 Evaluation of Results

Upon the estimation of GRD through natural targets, their accuracy is assessed by comparing them with the reference values derived from artificial targets. This evaluation employs the Root Mean Square Error (RMSE), in Eq. 8.

[5] LSF is normalized within the range of [0-1] by subtracting the minimum LSF value from each LSF value and then dividing the result by the difference between the maximum and minimum LSF values.

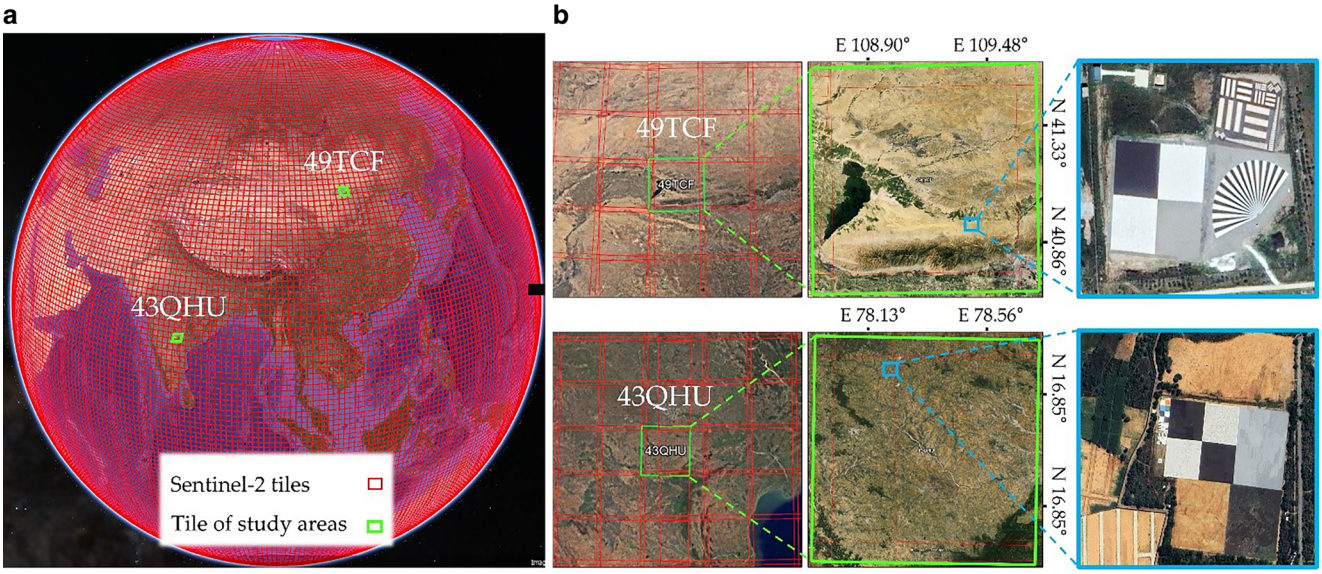

Fig. 4 Study areas: **a** overview of locations of two tiles containing Baotou and Shadnagar spatial calibration sites within the Sentinel tiling grid system, **b** Zoomed views of Baotou and Shadnagar sites within the 49TCF (up) and 43QHU (down) tiles, respectively. Subfigure (**a**) is a presentation of "S2A_OPER_GIP_TILPAR_MPC__20151209T095117_V20150622T000000_21000101T000000_B00.kml", openly accessible at https://sentiwiki.copernicus.eu/web/s2-documents

RMSE quantifies the extent to which the GRD estimated from natural targets deviates from the reference values.

$$RMSE = \sqrt{\frac{\sum_{i=1}^{X} (GRD_{NT} - GRD_{AT})^2}{X}} \tag{8}$$

where i denotes the natural target counter, X stands for the total number of natural targets, GRD_{NT} indicates the GRD value acquired from natural targets, and GRD_{AT} signifies the GRD value obtained from the artificial target. It is noteworthy that for each data there is only one GRD_{AT} value.

The precision of the GRD values is evaluated using the standard deviation (or variance) for each band using Eq. 9. The standard deviation tends to be lower when the GRD

Fig. 5 Sentinel-2 dataset in the true-color composite presentation: (**a**) Baotou site, and (**b**) Shadnagar site

Table 1 Information related to the Shadnagar and Baotou calibration sites

Site name	Location	Center Lat/Lon (°)	UTM Zone	Altitude above sea level (m)	Description and usability
Shadnagar	Hyderabad, Telangana, India, Asia	N 17.034/E 78.183	44	618	This target has four 70-m edge squares (the total dimension of 140 m × 140 m) and is rotated 5° east of true North. It is useful for RER assessments and estimating LSF and MTF in high- and medium-resolution RS systems. The Shadnagar site is located in a flat area, with an elevation difference of about 576 m between the highest and lowest points within the tile
Baotou	Baotou City, Inner Mongolia, China, Asia	N 40.854/E 109.628	49 *N*	1300	The Baotou CalVal Site features a 48 m × 48 m knife-edge square target (the total dimension of 96 m × 96 m) with gravel cover providing 5:1 contrast. Set at 5° angle to true North, the quadrants are gray, black, or white. This site is located in a tile with 1070 m elevation difference between the northern and southern mountains

Table 2 Information on Sentinel-2 dataset from the Shadnagar and Baotou study areas

Site	Data name	Satellite platform	Instrument (sensor)	Tile ID	Sensing time	Cloud cover (ratio)	Processing level
Baotou	S2A_MSIL2A_20230526T033541_N0509 _R061_T49TCF_20230526T070458	SENTINEL-2A	MSI	49TCF	2023-05-26T03:35:41.024Z	1.01E-1	S2MSI2A
Shadnagar	S2B_MSIL2A_20230528T050659_N0509 R019_T43QHU_20230528T074759	SENTINEL-2B	MSI	43QHU	2023-05-28T05:06:59.024Z	3.0E-6	S2MSI2A

values are more consistent (i.e., have closer values to each other), and vice versa.

$$\sigma_b = \sqrt{\sum_{i=1}^{X} \frac{\left(GRD_{NTi} - \overline{GRD}_{NT}\right)^2}{X-1}} \tag{9}$$

where σ_b is the standard deviation for each VNIR band, i represents the natural target counter, GRD_{NTi} refers to the GRD value obtained from the ith target, and $\overline{GRD}_{NT}$ denotes the mean value of all GRD observations from targets.

3.3 Study Areas and Datasets

Numerous spatial resolution calibration targets have been developed by aerospace and RS organizations worldwide to assess the ground resolution of aerial and high-resolution satellite images (Bushahab et al. 2014; Choi et al. 2019). Out of which, two prominent targets, namely the Shadnagar CalVal and Baotou targets, offer the potential for evaluating GRD in medium-resolution satellite imagery, particularly in the context of our study with Sentinel imagery[6]. Figure 4 illustrates the locations of these targets as two study areas, with details in Table 1.

Drawing from the dimensions of the Shadnagar and Baotou artificial tarps as the most sizable one among the existing targets, this study utilizes two tiles of Sentinel-2 imagery from the Shadnagar CalVal and Baotou calibration sites. Each tile covers an area of $100 \times 100\,\text{km}^2$ on Earth (Fig. 4). The datasets are multispectral surface reflectance, the L2A product. Figure 5 shows these datasets and Table 2 provides information.

4 Results

Following the workflow outlined in Fig. 1, the experiments are conducted in two modes: the primary mode, central to this research, focuses on estimating the ground resolution of Sentinel tiles using various natural targets; while a secondary mode involves artificial targets to assess the accuracy of the first mode.

4.1 Estimation of GRD Using Natural Targets

The proposed method for calculating GRD based on natural targets was applied to both datasets. The Canny operator was employed to extract image edges, followed by a Hough transform to detect lines. We manually selected appropriate straight line candidates (image subsets containing these lines) for GRD calculation, eliminating unsuitable ones. The extracted edges are displayed in Fig. 6.

Based on the edge maps, initial Hough lines were extracted from the Shadnagar and Baotou images, with numbers reported in Table 3. The final selection of lines, following human supervision, is presented in Fig. 7, along with statistics on their number and length (Table 3). After filtering, 40 lines were retained across both datasets.

Figure 8 showcases a collection of natural target image subsets in all four VNIR bands. These subsets have been cropped from each band. They are eligible edges that exhibit step-edge behavior. A straight line divides two uniform regions: one very dark and the other very light in color tone. There are no mixed pixels neighboring the straight lines; in other words, all pixels are uniform and pure.

The subsets containing these 40 lines exhibit the characteristics of an artificial target. They show a notable contrast in DN values perpendicular to the Hough lines, demonstrating proper spectral properties. These characteristics enable the generating of image LSF. Of the 40 extracted edges, five samples from each data are presented in Fig. 8.

For each selected natural target, sub-pixel edge locations were determined, from which edge profiles were extracted to derive ESF (detailed in Sect. “Material and Methods”). After normalizing the ESF profile, the FWHM was calculated and multiplied by the GSD to estimate the GRD. This process was repeated across all 40 natural targets.

The snapshots illustrating the GRD computation process were presented in Fig. 9 and 10 for the Shadnagar and Baotou case studies, respectively. One natural target exemplifies the process in each case.

Besides profile length, the number of profiles is also significant. Our rationale for determining the number of profiles is that it should be proportional to the number of pixels through which the least-squares fitted line passes. For n pixels under the fitted line, n profiles suffice. Given that the selected targets have pure pixels, lower values are also acceptable, but for those who prefer caution, we recommend determining the number based on the mentioned rationale.

The procedure depicted in Fig. 9 and 10 is applied to all 40 natural targets. The RMSE of residuals from the least-squares line fitting are reported in Table 4. The GRD results for each natural target are compiled in Table 5, alongside mean GRD values for each case study. The values exhibit consistency.

Beyond Table 5, statistical analysis is shown in the Box & Whisker plots of Fig. 11. The plots show the distribution of the GRD values, with the minimum, maximum, first quartile (Q1), median (Q2), and third quartile (Q3) for both case studies. In the figure, the minimum and maximum values represent the lower and upper extremes of each chart.

[6] Zuunmod in Mongolia, Songshan in China, Salon de Provence in France, Peng-Hu in Taiwan, Stennis in the USA, and FGI Sjökulla Aerial Test Range in Finland have smaller dimensions ($70\,\text{m} \times 70\,\text{m}$), making them unsuitable for medium- and low-resolution satellite imagery.

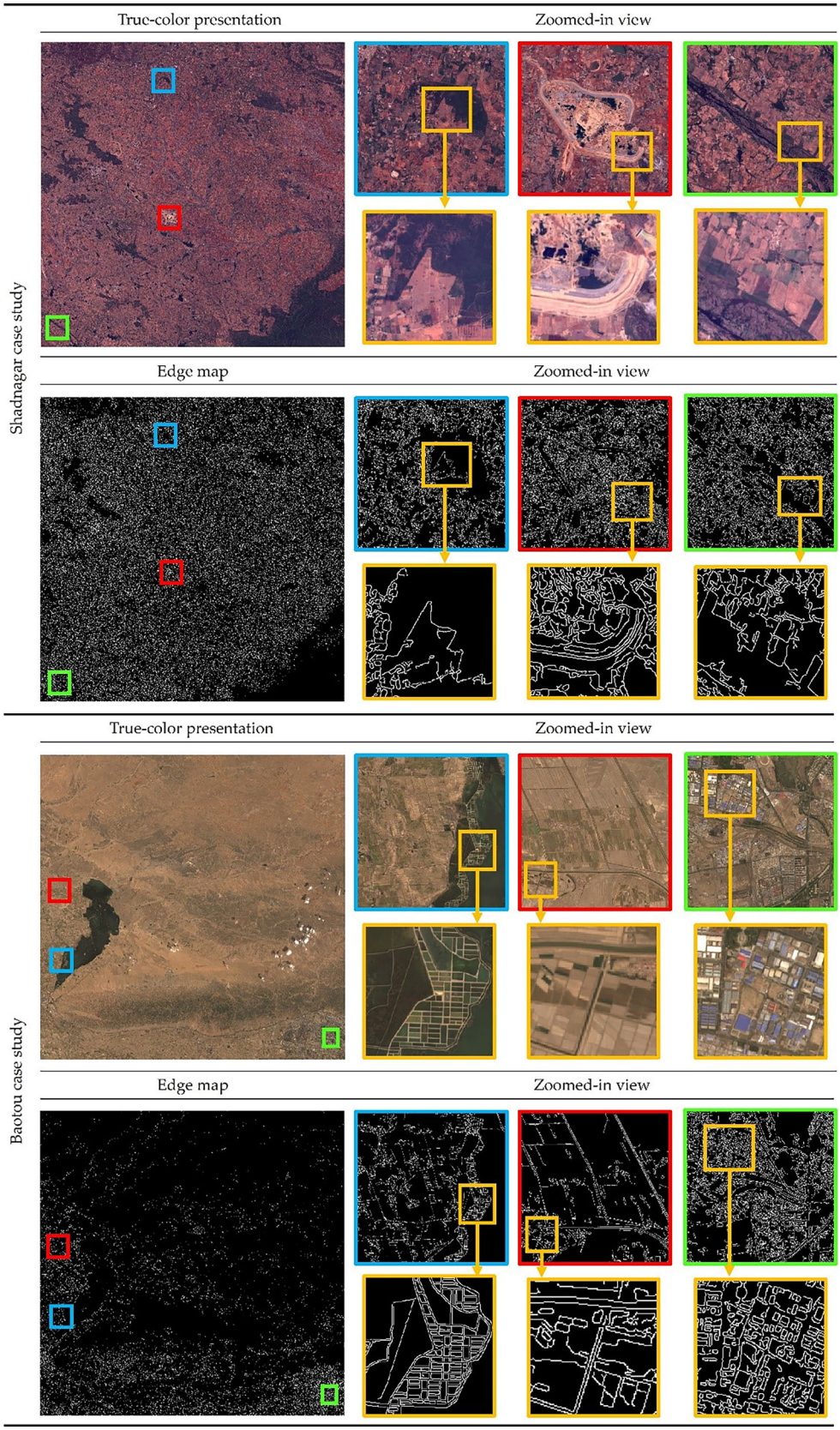

Fig. 6 Primary edge extraction results (edge maps) in two case studies

Table 3 Statistical summary of the extracted and selected lines

Case study	Number of extracted lines	Number of selected lines	Length of selected lines (pixel)
Shadnagar	34	20	Min = 11, Max = 52, Mean = 20
Baotou	41	20	Min = 12, Max = 53, Mean = 24

Q1 and Q3 denote the lower and upper bounds of each box, with Q2 indicated by a horizontal line within each box.

4.2 Estimation of GRD Using Artificial Targets

Given the 10-m GSD of Sentinel imagery in the VNIR bands, as well as the dimensions of existing calibration targets worldwide, two of the largest targets were chosen for experimental testing: the Shadnagar CalVal tarp and the Baotou calibration tarp. Other targets' dimensions do not provide enough pixels perpendicular to the edge direction. to generate ESF, LSF, FWHM, and GRD accurately. Thus, these targets were not used.

This section was implemented separately for each of the 10-m VNIR bands of the target, proceeding band by band. Subpixel edge locations were extracted from a manually acquired target subset. A line was fitted to edges within one panel, from which profiles were generated to record

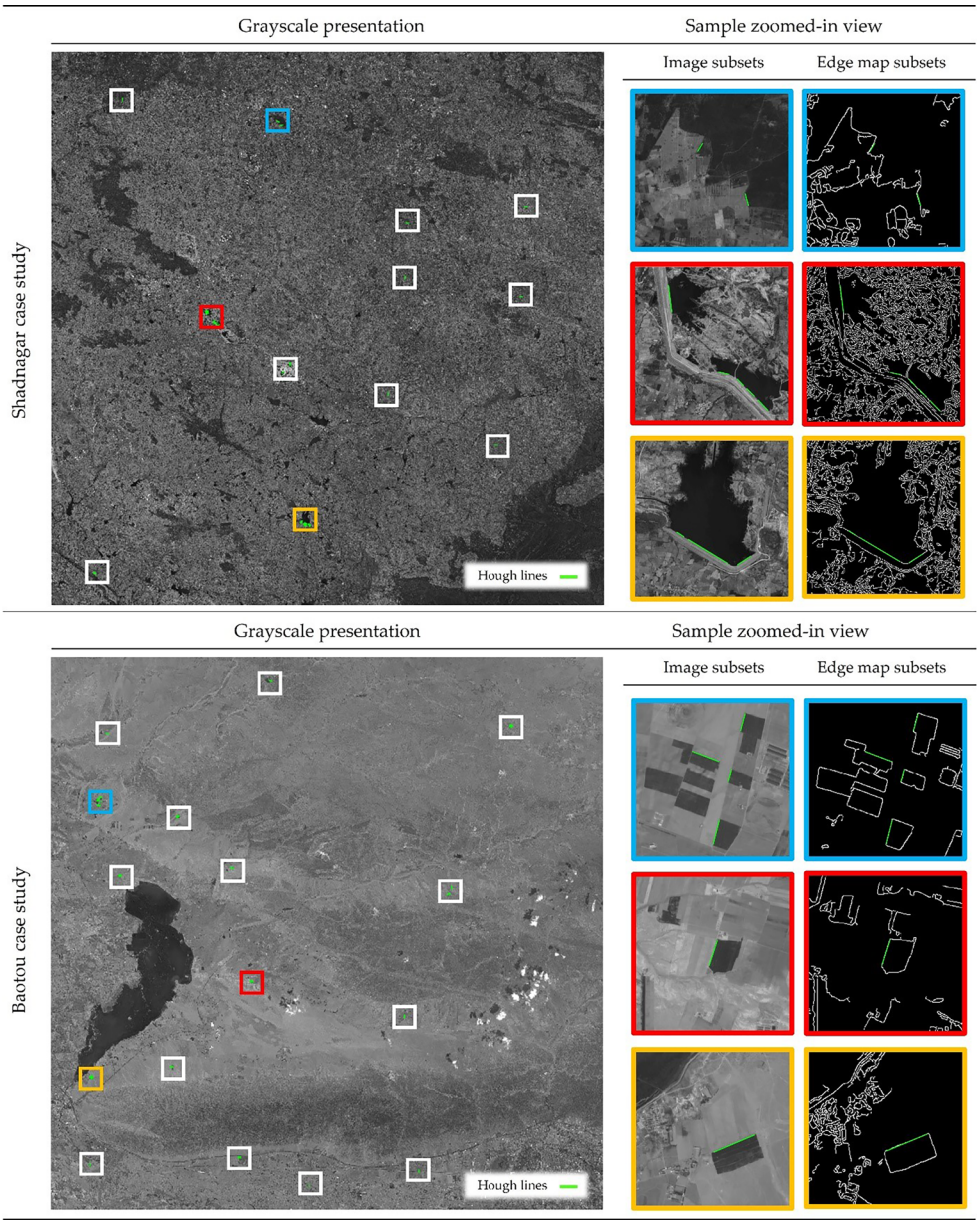

Fig. 7 Hough line extraction results in two case studies

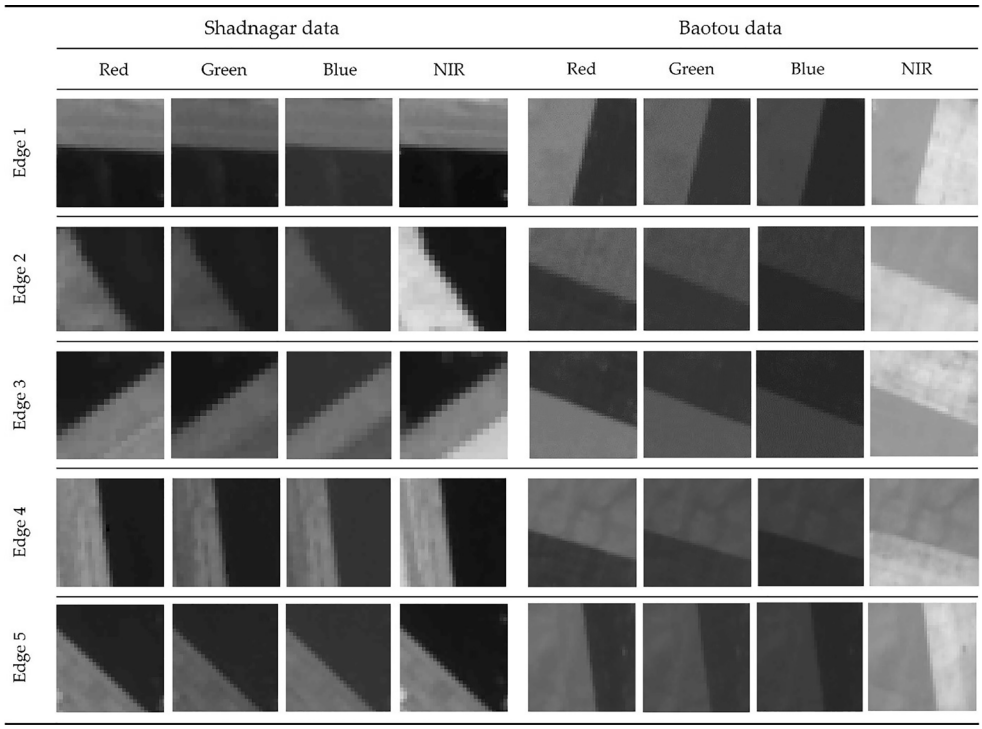

Fig. 8 Samples of selected image subsets (natural targets) with eligible edges in both datasets

DN values. The ESF was derived, enhanced through linear interpolation, and used to estimate the LSF. Finally, the FWHM was calculated and multiplied by the GSD of VNIR bands to determine the GRD.

The results of GRD estimation for the VNIR bands are depicted in Fig. 12 for Shadnagar and Fig. 13 for Baotou. A similar process has been done for the other three edges and the average values are obtained. Based on the FWHM values, the estimated GRD values for the red, green, blue, and NIR bands of the Shadnagar dataset are 13.61 m, 13.39 m, 13.56 m, and 13.72 m, respectively. For Baotou, the GRD values are 12.19 m, 11.70 m, 12.91 m, and 12.06 m.

5 Discussions

We can assess both the accuracy and precision of the GRD values derived from natural targets and discuss the feasibility of the scene-driven approach for estimating Sentinel GRD. To evaluate the accuracy, the results from natural targets were compared against artificial targets, providing insights into the degree of deviation.

Table 6 presents mean GRD values derived from natural targets (GRD_{NT}), the corresponding values from artificial targets (GRD_{NT}), the absolute difference, and RMSE values, which serve as indicators of accuracy for each band. Results show a close alignment between GRD values obtained from natural targets and those from artificial targets, with an overall RMSE of 0.77 m.

The performance of natural targets in estimating the GRD of Sentinel-2 imagery is satisfactory, with an average RMSE of <0.8 m. Given the GSD of VNIR bands (10 m), this error is acceptable, suggesting natural targets are suitable for GRD estimation in tiles lacking artificial targets.

For the precision of GRD results from natural targets, the standard deviation was computed for each band (Table 6). Results show a slight variability across bands. The blue bands showed less consistency, with an average standard deviation of 0.255 m in the two case studies. The red band had the most consistency, with an average standard deviation of 0.161 m.

Despite slight variations, attributed to factors such as errors in edge detection and line fitting, the GRD values from natural targets remain consistent. The overall precision of the mean value of 0.199 m across all bands, confirms the effectiveness of natural targets in estimating GRD in Sentinel imagery. Thus, the proposed scene-driven method demonstrates both accuracy and precision.

Our semi-automatic edge detection approach is an advancement compared to Li et al. (2014) and Kim et al. (2008). Unlike manual edge selection on limited image subsets from specific parts of the scene in prior studies, our method offers a more efficient edge detection process. It assesses the GRD for the entire image, giving a realistic average estimation for the whole scene. However, in medium-resolution imagery, the difficulty in accurately detecting edges remains challenging. To mitigate error effects and improve the accuracy of edge detection, we adopted the high-end sub-pixel edge location extraction method by

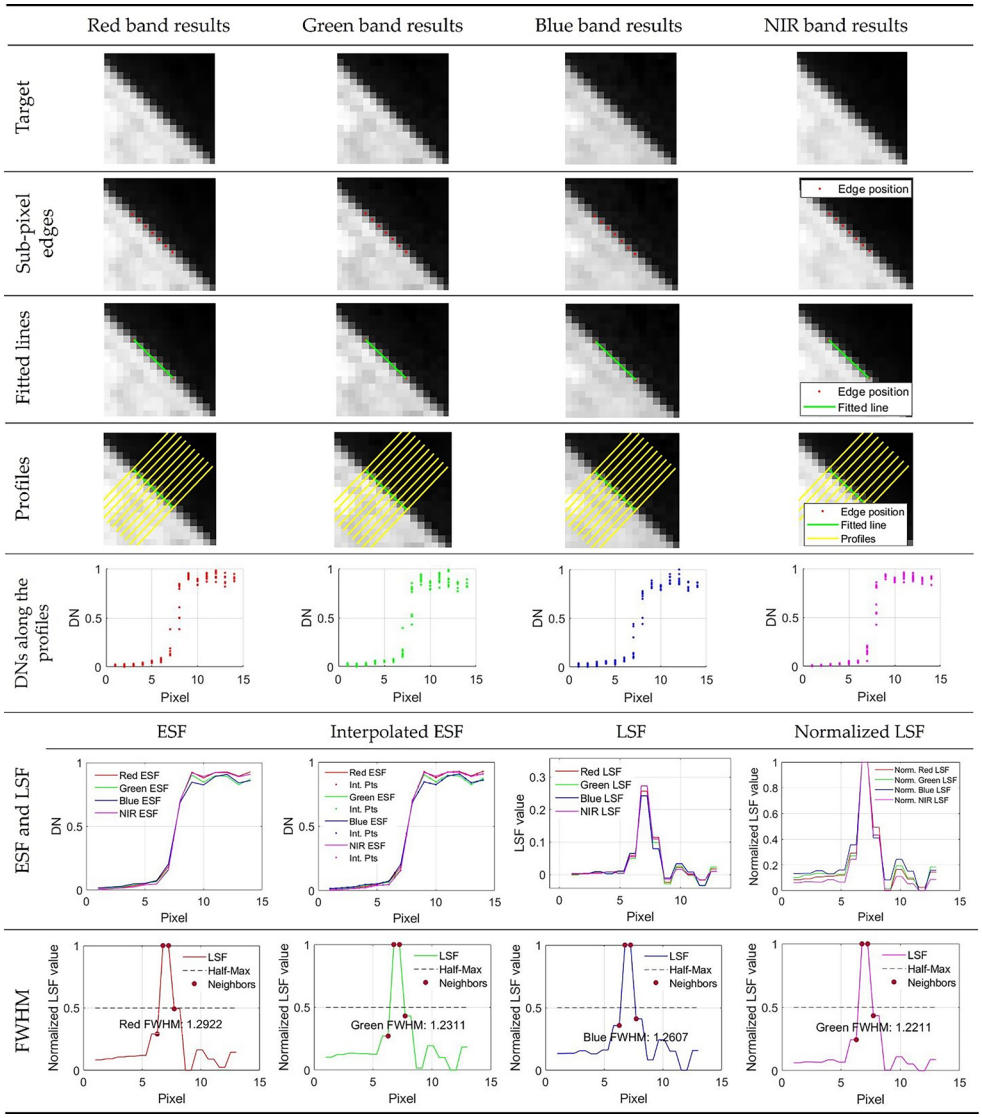

Fig. 9 GRD estimation process for a sample natural target in the Shadnagar case study

Trujillo-Pino et al. (2013). Despite its usefulness, it requires attention to potential errors that may arise.

Our edge analysis-based method for estimating GRD in Sentinel (and other medium-resolution imagery) faces the limited dimensions of natural targets, limiting the number of pixels perpendicular to the edge orientation. We utilize maximum pixels to create profiles. This ensures that the ESF is generated from an adequate number of pixels, accurately representing the behavior of edges. While profile length is recognized as crucial in higher resolution assessment (Javan et al. 2013), it is more critical here due to low GSD.

Accurate edge location detection is crucial as it forms the foundation of our edge analysis-based method, necessitating attention to potential errors during the initial step. Even one inaccurately detected edge point can impact the least-squares fitted line. This affects ESF and LSF affecting FWHM and GRD.

Due to the significance of this issue, this study introduces a novel approach to assess the sensitivity of GRD calculations to sub-pixel variations in edge positions. The methodology begins with sub-pixel edge detection on a natural target and then introduces controlled, random directional sub-pixel shifts to the detected positions. These shifts are applied in eight cardinal and intercardinal directions, with magnitudes incrementally increasing across iterations. For each iteration, the GRD is recalculated based on the shifted edge positions. This analysis quantifies changes in GRD relative to the initial, unshifted calculation, providing insights into the robustness of GRD estimation under varying edge detection accuracy.

For a target with an initial GRD of 12.593 m, a maximum sub-pixel shift of 1 m was applied to all edge positions randomly. The impact of these variations is presented in Fig. 14. The results show that the mean (maximum) rel-

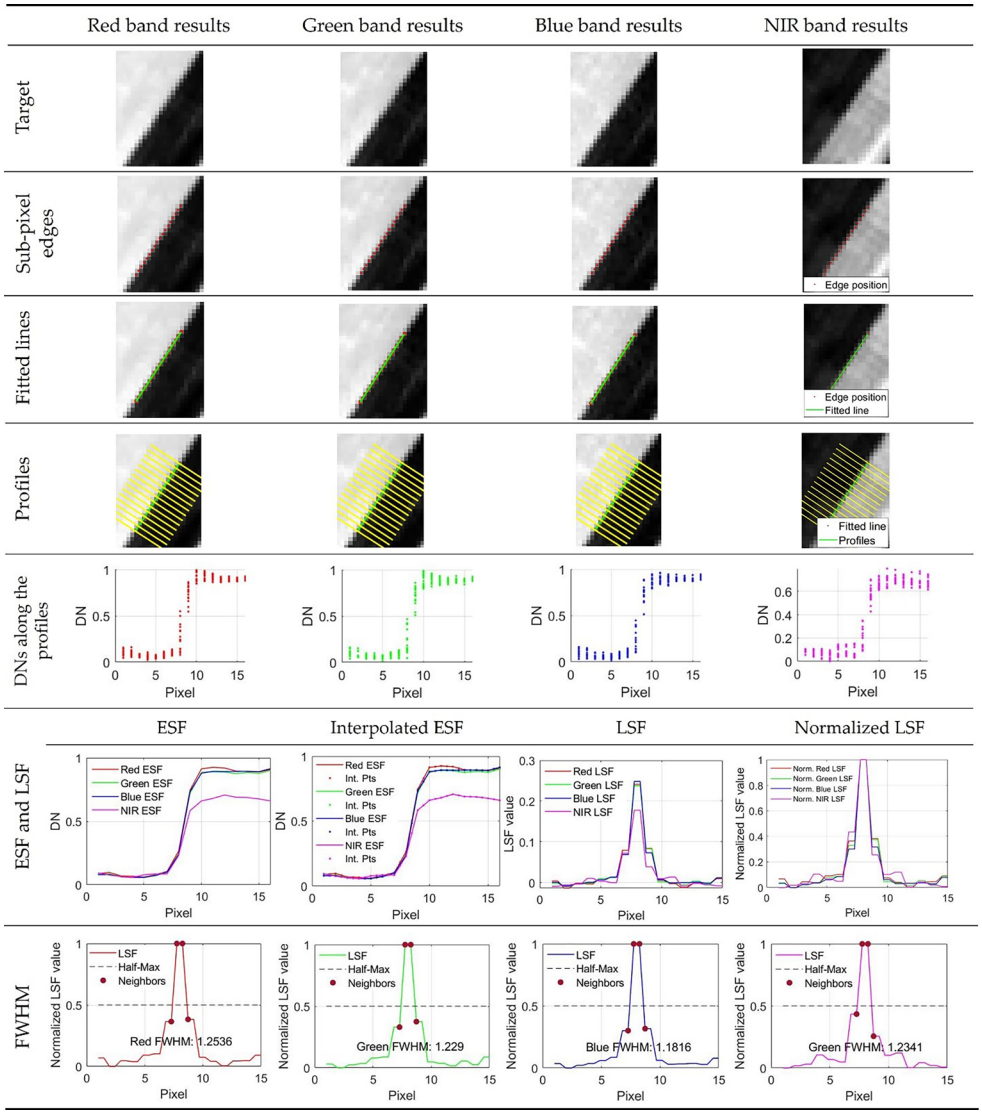

Fig. 10 GRD estimation process for a sample natural target in the Baotou case study

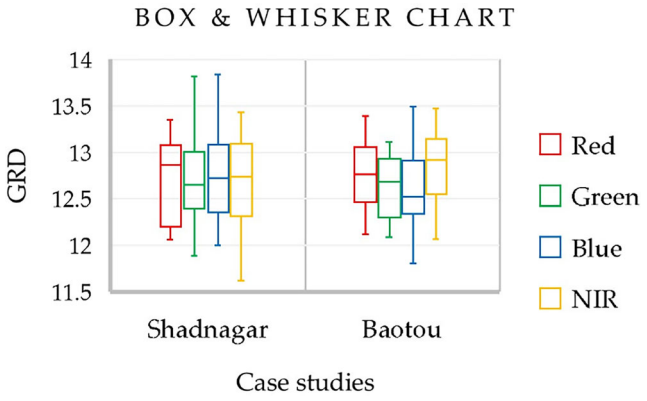

Fig. 11 Statistical summary of GRD values of VNIR bands in two case studies

ative change in GRD was 0.60% (10.73%), corresponding to a mean (maximum) change of 0.076 m (1351 m).

An important aspect to note is that our method relies on official reports from the ESA and information provided in existing papers, such as Drusch et al. (2012), which detail the specifications of the Sentinel RS system. The GSD for the VNIR bands is specified as 10 m for the nadir regions. However, there may be slight variations in GSD values for off-nadir areas (given Sentinel's large field of view), which can influence GRD. Thus, averaging GRD results from natural targets across the tile (both nadir and off-nadir areas) is the most reasonable solution to accurately reflect the ground resolution. Our method operates under the assumption that the GSD provided by ESA in the metadata, accurately reflects a GSD of 10 m for the VNIR bands.

GRD in satellite imagery may vary slightly in two directions: along-track and across-track (Cenci et al. 2021; Pampanoni et al. 2024). In our study, while Hough lines

Table 4 RMSE (pixel) of the residuals in LS line fitting

	Shadnagar data				Baotou data			
NTs	Red	Green	Blue	NIR	Red	Green	Blue	NIR
NT1	0.0194	0.0275	0.0317	0.0135	0.0713	0.0804	0.0864	0.0989
NT2	0.2502	0.1461	0.2672	0.1500	0.0935	0.0967	0.1069	0.1177
NT3	0.1227	0.1954	0.2094	0.1198	0.0917	0.0963	0.1260	0.1006
NT4	0.1378	0.0816	0.1770	0.1728	0.1662	0.2802	0.2363	0.4357
NT5	0.0938	0.0849	0.1312	0.0579	0.0386	0.0479	0.0644	0.1600
NT6	0.0454	0.0179	0.0879	0.1929	0.0408	0.0345	0.0420	0.0705
NT7	0.0739	0.0607	0.1242	0.0732	0.1437	0.1412	0.1351	0.1484
NT8	0.1888	0.2521	0.1215	0.1116	0.0690	0.0627	0.0661	0.0422
NT9	0.0940	0.0425	0.0755	0.0750	0.0483	0.0613	0.0527	0.1061
NT10	0.1224	0.1036	0.1570	0.1411	0.0388	0.0437	0.0312	0.1752
NT11	0.0694	0.0399	0.0999	0.1081	0.0524	0.0858	0.0767	0.0701
NT12	0.1664	0.2191	0.2877	0.2530	0.0950	0.0957	0.1124	0.1129
NT13	0.0487	0.0518	0.0401	0.0373	0.1061	0.1901	0.1406	0.0691
NT14	0.0851	0.0823	0.1096	0.0653	0.4638	0.2932	0.4462	0.1991
NT15	0.1259	0.1054	0.1382	0.2083	0.1004	0.1239	0.1104	0.1745
NT16	0.0242	0.0165	0.0445	0.0268	0.1492	0.1135	0.1420	0.5041
NT17	0.1397	0.1287	0.1133	0.0690	0.5803	0.6951	0.5155	0.2779
NT18	0.1156	0.1374	0.1776	0.1022	0.8402	0.3457	0.6312	0.2177
NT19	0.0840	0.1212	0.1212	0.0407	0.0981	0.1024	0.1464	0.0843
NT20	0.1469	0.1507	0.0923	0.0534	0.1750	0.1985	0.1444	0.3222
Mean	0.1077	0.1033	0.1304	0.1036	0.1731	0.1594	0.1706	0.1744

Table 5 GRD (m) estimation results for natural targets (NTs) in VNIR bands of two datasets

	Shadnagar data				Baotou data			
NTs	Red	Green	Blue	NIR	Red	Green	Blue	NIR
NT1	12.91	12.39	12.65	12.34	13.06	12.74	12.38	12.95
NT2	13.19	12.81	13.84	13.03	13.39	12.29	12.50	12.63
NT3	12.94	13.82	13.40	12.96	12.82	12.51	11.96	12.28
NT4	12.81	12.67	13.06	13.10	13.38	13.11	13.49	12.96
NT5	12.20	12.61	12.26	13.05	13.06	12.67	12.71	12.99
NT6	12.87	13.01	12.57	12.65	12.53	12.29	11.81	12.34
NT7	12.06	12.63	12.00	12.16	12.58	12.33	13.06	12.07
NT8	13.10	13.32	12.30	12.79	12.78	12.95	12.43	12.69
NT9	12.86	12.62	12.53	13.43	12.76	12.58	12.22	13.10
NT10	13.35	13.68	13.26	13.34	12.44	12.22	12.95	13.40
NT11	13.13	12.99	13.03	13.31	12.76	12.69	12.79	12.95
NT12	12.14	12.17	12.79	12.62	12.58	12.83	12.55	13.27
NT13	12.13	12.71	13.09	12.55	13.08	12.84	13.15	13.23
NT14	12.58	12.91	12.62	12.68	12.18	13.01	12.40	13.47
NT15	12.20	11.89	11.24	11.78	12.31	12.10	12.56	13.16
NT16	12.92	12.31	12.60	12.21	12.12	12.92	13.29	12.89
NT17	13.28	12.53	12.96	13.15	12.83	13.06	12.19	12.57
NT18	12.81	13.36	13.09	12.99	12.64	12.93	12.38	12.37
NT19	13.01	12.40	12.11	11.62	12.25	12.09	12.33	12.54
NT20	12.16	12.29	12.90	12.31	13.12	12.56	12.61	12.79
Mean	12.74	12.76	12.71	12.70	12.73	12.64	12.59	12.83

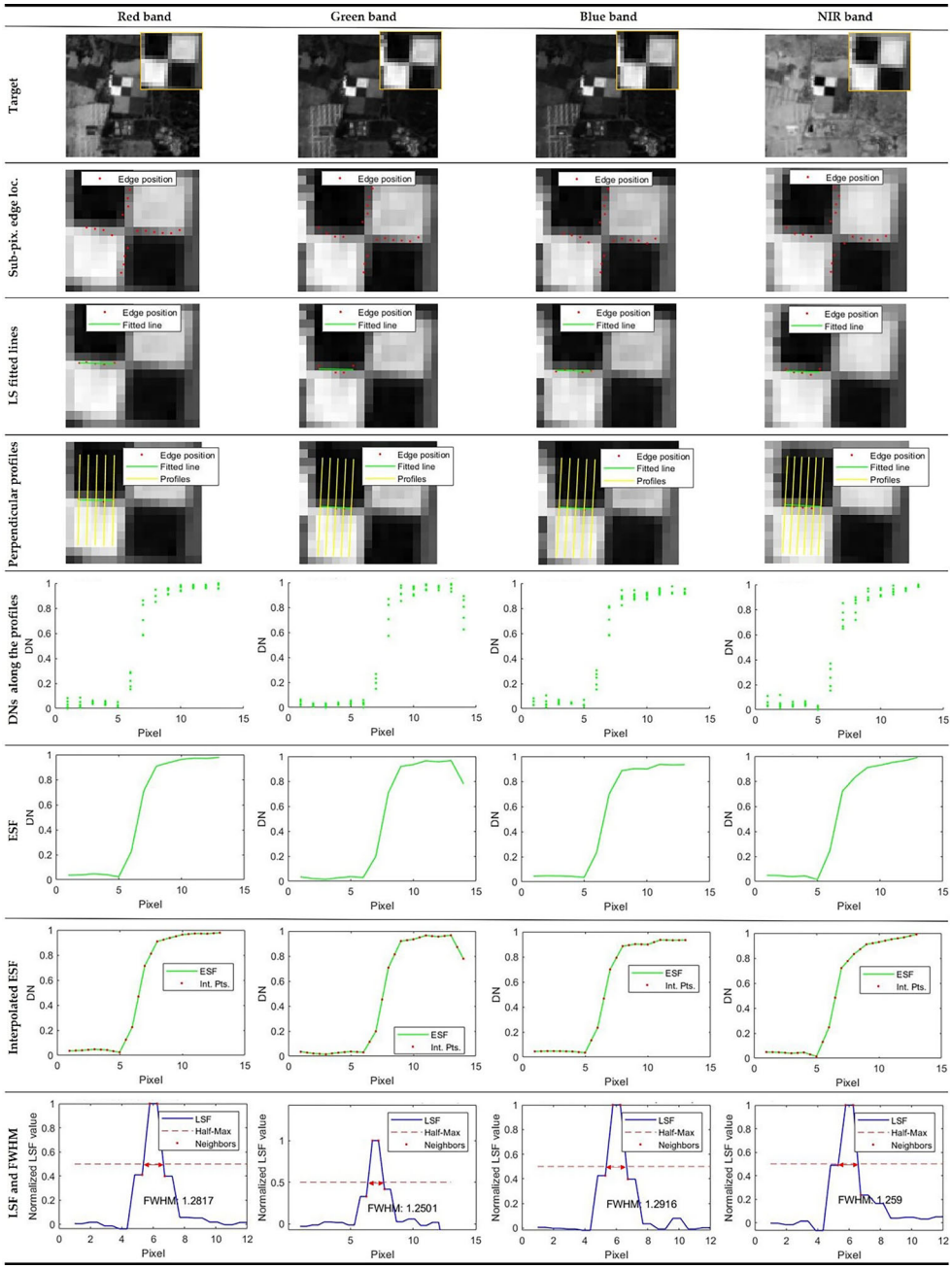

Fig. 12 GRD calculation in VNIR bands using Shadnagar target

Table 6 Accuracy and precision assessment of GRD obtained from natural targets

	Shadnagar				Baotou			
	GRD_{NT}(m)	GRD_{AT}(m)	|Δ|(m)	σ(m)	GRD_{NT}(m)	GRD_{AT}(m)	|Δ|(m)	σ(m)
Red	12.74	13.61	0.87	0.184	12.73	12.19	0.54	0.139
Green	12.76	13.39	0.63	0.247	12.64	11.70	0.94	0.106
Blue	12.71	13.56	0.85	0.323	12.59	12.91	0.32	0.189
NIR	12.70	13.72	1.02	0.259	12.83	12.06	0.77	0.152
Mean	12.73	13.57	0.84	0.253	12.69	12.26	0.43	0.147
RMSE(m)	–	–	0.85	–	–	–	0.68	–

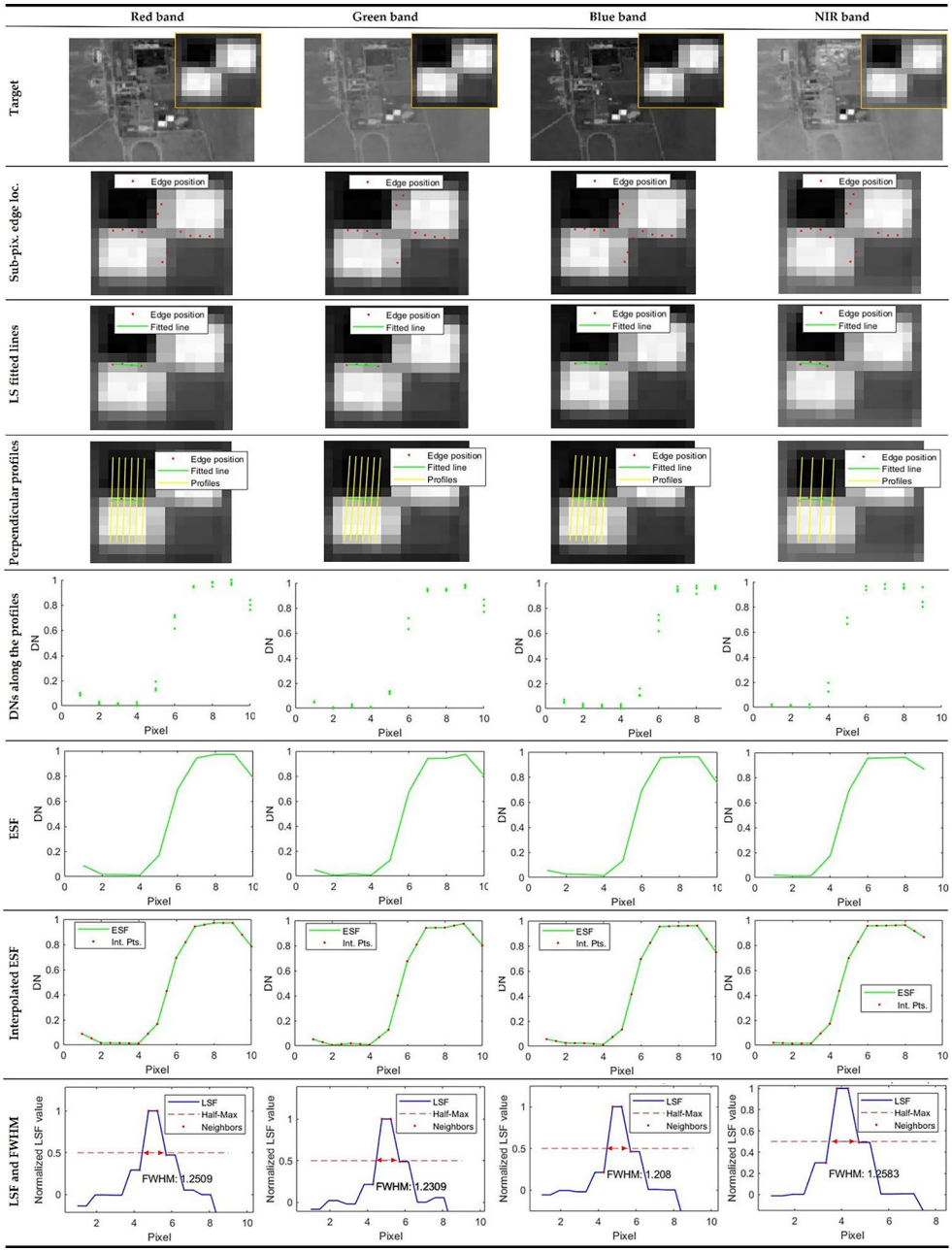

Fig. 13 GRD calculation in VNIR bands using Baotou target

are present in all directions, the effects of edge directions have not been separately investigated. However, the average GRD reflects the combined impact of both directions simultaneously. Following the findings of Pampanoni et al. (2024), who observed no significant differences in edge directions (e.g., along-track and across-track) in their automatic edge detection method applied to medium-resolution satellite imagery, our research doesn't categorize results based on edge orientation.

In our investigation of edge direction, we examined two classes of edges: aligned with the satellite's path (along-track) and perpendicular to it (across-track). Using metadata from the Shadnagar and Baotou datasets, we determined that for Sentinel-2, which employs a pushbroom sensor and moves in a descending orbit (north to south), the along-track direction is north-south, while the across-track is east-west. We classified horizontal edges (east-west) as across-track and vertical edges (north-south) as along-track. Our analysis, presented in Fig. 15, encompasses four along-track and four across-track targets from two datasets. The results do not indicate a consistent pattern of GRD being larger in either the across-track or along-track direction. This finding aligns with Pampanoni et al. (2024), suggesting that edge direction doesn't systematically influence spatial resolution.

Supporting previous works, by Cenci et al. (2021), Javan et al. (2013), Kim et al. (2008, 2010a, b), Kim and

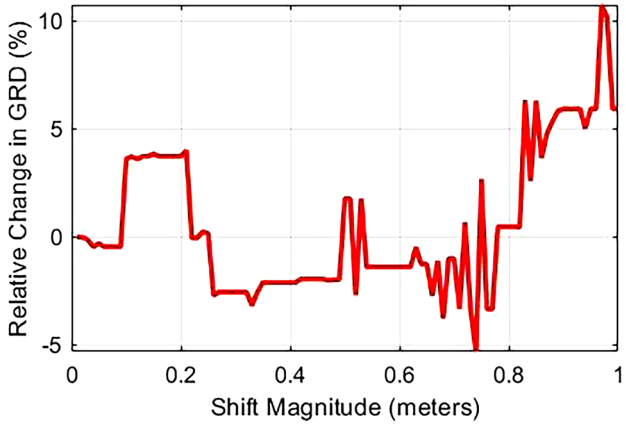

Fig. 14 Impact of sub-pixel edge position variation on GRD

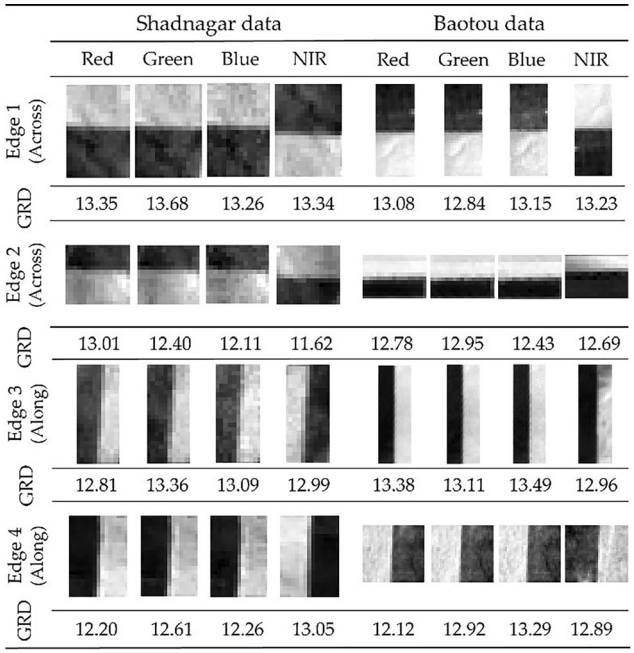

Fig. 15 Impact of edge direction on GRD

Kim (2011a, b), Li et al. (2014), and Pampanoni et al. (2020, 2022, 2024), regarding the feasibility of using natural targets for resolution estimation our research confirms that carefully chosen targets support resolution assessments, following to the guidelines outlined.

Our research doesn't align with the findings of Pampanoni et al. (2024), who discussed the relationship between sharpness, spatial resolution, and SNR of satellite images in terms of the mean value (μ) of FWHM. Their FWHM values are higher than those observed in our study. Their results were not validated using calibration targets, and no representation of the automatically extracted edges was provided to assess the quality and types of edges. This discrepancy could be attributed to several factors, notably the total number of edges included in their analysis, which is higher than ours. Due to the semi-automatic nature of our method, we are confident that all natural targets exhibit the characteristics of a calibration target, both in terms of having a straight, step-like edge and spectral characteristics. Their automatic target detection method relies on thresholds of DN values, so there is no guarantee that all targets have pure pixels, as one or more mixed pixels may affect the results. We couldn't confirm the existence of as many targets as reported by them within the Sentinel imagery. Since each target should have eligible edges for all bands, finding a target that could be eligible in VNIR bands is challenging, and such targets are seldom found. As there is no representation of their edge-based analysis, especially the numerous edges, and they are not compared with calibration targets, we can't explicitly comment on their contributions and the differences with ours.

To examine the position dependency of GRD, specifically to identify potential variations across the image, three target classes—left, nadir, and right—were analyzed, assuming along-track positioning has no effect. For this analysis, the two Sentinel images were divided into three sections: left, center, and right. Targets were then categorized based on their placement in one of these sections. The results are presented in Table 7.

The analysis revealed spatial variations across the sensor's field of view, with consistently higher GRD values in the center position. For the Shadnagar site, the center position exhibited a mean GRD of 12.85 ± 0.13 m, higher than the left (12.63 ± 0.09 m) and right positions (12.65 ± 0.07 m). Similarly, at the Baotou site, the center position showed a mean GRD of 12.84 ± 0.13 m, exceeding both left (12.75 ± 0.07 m) and right positions (12.49 ± 0.10 m).

6 Conclusions

This study addressed the resolution of one of the most widely used satellite imagery, namely Sentinel-2. We proposed a semi-automated scene-driven approach to estimate GRD as an alternative to GSD. The feasibility of utilizing natural targets for estimating GRD in Sentinel-2 imagery was verified using calibration targets within the same tile. The GRD estimation method demonstrated an average RMSE of 0.77 m and a total standard deviation of 0.19 m. Natural targets, with straight edges and spectral contrast, can effectively be used in evaluating GRD in satellite imagery, particularly Sentinel-2 imagery.

The average GRD for Sentinel-2 surface reflectance cloud-free product was determined as 12.65 m, 12.40 m, 12.49 m, and 12.58 m for the red, green, blue, and NIR bands, respectively, based on two tiles featuring artificial targets in Shadnagar and Baotou. Considering the GSD of

Table 7 The position-dependency analysis of GRD (m)

	Shadnagar data			Baotou data		
	Left	Center	Right	Left	Center	Right
Red	12.69	12.81	12.71	12.94	12.85	12.61
Green	12.55	12.99	12.55	12.78	12.79	12.47
Blue	12.54	12.91	12.70	12.48	12.72	12.38
NIR	12.73	12.69	12.63	12.81	13.02	12.53
Mean	12.63	12.85	12.65	12.75	12.84	12.49
Std Dev	±0.09	±0.13	±0.07	±0.07	±0.13	±0.10

10 m, the ratio of GRD to GSD for these bands is 1.25. In an ideal scenario, this ratio could be as close as possible to 1. An ideal scenario would involve moderate weather conditions and minimal atmospheric particles.

Several avenues for future investigation remain. Firstly, estimating GRD values for other bands of Sentinel-2 using this methodology warrants exploration. This requires artificial calibration targets with larger dimensions, along with natural targets of increased size.

As a second research avenue, analyzing the spatial variation of GSD and GRD across different parts of a Sentinel tile warrants investigation. Due to Sentinel's large field of view, and considering that GRD is closely related to GSD, these metrics differ between the nadir and margin areas of the swath, being influenced by the satellite's yaw, roll, pitch angles, and its distance from the center of the field of view. While data providers typically report GSD values for the nadir area of the imagery, understanding how these metrics vary across different parts of the tile is not straightforward. Such analysis could determine whether these variations between center and margin areas are significant, quantify their magnitude, and identify underlying patterns.

Studies of the temporal changes of GRD values across different tiles acquired during various months of the year constitute a third research topic. Since factors like sunlight azimuth, air particle concentration, air density, and air temperature affect ground resolution, evaluating their impact on GRD provides valuable insights for the RS community.

This study computed GRD based on surface reflectance imagery that underwent atmospheric correction (L2A). Hence, a fourth research avenue could investigate the influence of atmospheric effects by calculating GRD using top-of-atmosphere (TOA) reflectance data and comparing the results with surface-reflectance products. L1A and L1B products are not available to users and there is no possibility to investigate their GRD. Since L2A and L1C products are resampled, future studies can investigate this resampling's impacts on the GRD.

Proposing a fully automated method for GRD evaluation of medium-resolution satellite imagery presents a fifth research opportunity. This could involve developing a method that automatically assesses the Hough lines' surroundings to ensure the presence of pure pixels and adequate contrast to exhibit step-edge behavior. The method should not only analyze edge surroundings in terms of DN values (as used by Cenci et al. (2021) and Pampanoni et al. (2020, 2022, 2024)) but also ensure the absence of mixed pixels in the subset area. Considering the similar concepts of NIIRS and GRD, future research could explore the potential of using natural targets for estimating NIIRS.

As noted in Table 1, we assessed two Sentinel tiles: one flat (Shadnagar) and one mountainous (Baotou). Topographic variations, especially in mountainous regions, may affect GRD, particularly at swath edges with large off-nadir angles. Future research could explore the impact of topography on GRD. No suitable targets with straight edges and spectral capability were found in mountainous areas.

In conclusion, this research provides a valuable contribution to the RS scientific community, particularly for those studying Sentinel-2 imagery where accurate GRD estimation is crucial. The methodology has broader applicability across various geospatial datasets, regardless of sensor type. It can be applied to coarser-resolution imagery including Landsat and finer-resolution datasets, e.g., commercial high-resolution satellite imagery and aerial images.

Funding No funding was received for conducting this study.

Author Contribution All authors contributed to the study conception and design. Material preparation, data collection and analysis were performed by F.D.J., F.S., and A.T. The first draft of the manuscript was written by A.T., and F.D.J., F.S., M.S., and C.P. commented on previous versions of the manuscript. All authors read and approved the final manuscript.

Availability of data and material The datasets generated during and/or analysed during the current study are available from the corresponding author on reasonable request.

Code availability Code used in this study is available from the corresponding author on reasonable request.

Conflict of interest F. DadrassJavan, F. Samadzadegan, A. Toosi, M. Schneider and C. Persello declare that they have no competing interests.

References

Banik B, Vukusic J, Stake J (2009) Millimeter wave characterization of a catadioptric lens for imaging applications. IEEE Microw Wirel Components Lett 19:680. https://doi.org/10.1109/LMWC.2009.2031997

Belgiu M, Csillik O (2018) Sentinel-2 cropland mapping using pixel-based and object-based time-weighted dynamic time warping analysis. Remote Sens Environ 204:509. https://doi.org/10.1016/j.rse.2017.10.005

Bushahab A, Al-Mansoori S, Al-Suwaidi K, Al Matroushi H, Al-Tunaiji E, Al Shamsi M (2014) Cal/val activities for DubaiSat-2 performance assessment sensors, systems, and next-generation satellites XVIII. SPIE 9241:319–327. https://doi.org/10.1117/12.2067593

Campbell JB, Wynne RH (2011) Introduction to remote sensing. Guilford

Canny J (1986) A computational approach to edge detection. IEEE Trans Pattern Anal Mach Intell 679:

Cenci L, Pampanoni V, Laneve G, Santella C, Boccia V (2021) Presenting a semi-automatic, statistically-based approach to assess the sharpness level of optical images from natural targets via the edge method. Case study: the landsat 8 oli–l1t data. Remote Sens 13:1593. https://doi.org/10.3390/rs13081593

Choi J, Park H, Seo D (2019) Pansharpening using guided filtering to improve the spatial clarity of VHR satellite imagery. Remote Sens 11:633. https://doi.org/10.3390/rs11060633

Clabaut É, Foucher S, Bouroubi Y, Germain M (2024) Synthetic data for sentinel-2 semantic segmentation. Remote Sens 16:818. https://doi.org/10.3390/rs16050818

Conran DN (2024) A new vicarious technique for radiometric and spatial calibration of drone-based multispectral and hyperspectral imaging systems. Rochester Institute of Technology

Cramer M, Zhang S, Meißner H, Reulke R (2020) Quality assessment of high-resolution UAV imagery and products. Proceedings of the 40. Wissenschaftlich-Technische Jahrestagung der DGPF in Stuttgart, vol 4. Stuttgart

Crespi M, De Vendictis L (2009) A procedure for high resolution satellite imagery quality assessment. Sensors 9:3289. https://doi.org/10.3390/s90503289

Dąbrowski R, Jenerowicz A (2015) Portable imagery quality assessment test field for UAV sensors. Int Arch Photogramm Remote Sens Spatial Inf Sci 40:117. https://doi.org/10.5194/isprsarchives-XL-1-W4-117-2015

Dabrowski R, Orych A, Jenerowicz A, Walczykowski P (2015) Preliminary results from the Portable Imagery Quality Assessment Test Field (PIQuAT) of UAV imagery for imagery reconnaissance purposes. Int Arch Photogramm Remote Sens Spatial Inf Sci 40:111. https://doi.org/10.5194/isprsarchives-XL-1-W4-111-2015

Drusch M, Del Bello U, Carlier S, Colin O, Fernandez V, Gascon F, Hoersch B, Isola C, Laberinti P, Martimort P (2012) Sentinel-2: ESA's optical high-resolution mission for GMES operational services. Remote Sens Environ 120:25. https://doi.org/10.1016/j.rse.2011.11.026

Dubey B, Sharma A, Prakash S, Darji NP, Dhar D (2024) Frequent oversights in on-orbit modulation transfer function estimation of optical imager onboard EO satellites. J Appl Rem Sens 18:36501. https://doi.org/10.1117/1.JRS.18.036501

Duda RO, Hart PE (1972) Use of the Hough transformation to detect lines and curves in pictures. Commun ACM 15:11

Ghassoun Y, Gerke M, Khedar Y, Backhaus J, Bobbe M, Meissner H, Tiwary PK, Heyen R (2021) Implementation and validation of a high accuracy UAV-photogrammetry based rail track inspection system. Remote Sens 13:384. https://doi.org/10.3390/rs13030384

Javan FD, Samadzadegan F, Reinartz P (2013) Spatial quality assessment of pan-sharpened high resolution satellite imagery based on an automatically estimated edge based metric. Remote Sens 5:6539. https://doi.org/10.3390/rs5126539

Joseph G (2005) Fundamentals of remote sensing. Universities press

Kim J-I, Kim T-J (2011a) Development of a natural target-based edge analysis method for NIIRS estimation. Korean J Remote Sens 27:587. https://doi.org/10.7780/kjrs.2011.27.5.587

Kim T, Kim J (2011b) Automated assessment of NIIRS and GRD of high resolution satellite images through edge profile analysis of natural targets. Civil Commercial Imagery Evaluation Workshop

Kim J-I, Jeong J-H, Kim T-J (2010a) Development of GRD measurement method using natural target in imagery. Korean J Remote Sens 26:527

Kim T, Kim H, Kim H (2008) Image-based estimation and validation of NIIRS for high-resolution satellite images. Int Arch Photogramm Remote Sens Spatial Inf Sci 37:1

Kim T, Kim J, Kim D, Jeong J (2010b) Automated image interpretability assessment by edge profile analysis of natural targets. Oppor Emerg Geospatial Technol

Kubišta J, Surový P (2021) Spatial resolution of unmanned aerial vehicles acquired imagery as a result of different processing conditions. Cent Eur For J 67:148. https://doi.org/10.2478/forj-2021-0011

Lasko K, O'Neill FD, Sava E (2024) Automated mapping of land cover type within international heterogenous landscapes using sentinel-2 imagery with ancillary geospatial data. Sensors 24:1587. https://doi.org/10.3390/s24051587

Leachtenauer JC, Malila W, Irvine J, Colburn L, Salvaggio N (1997) General image-quality equation: GIQE. Appl Opt 36:8322. https://doi.org/10.1364/AO.36.008322

Lee J-H, Sull S (2019) Regression tree CNN for estimation of ground sampling distance based on floating-point representation. Remote Sens 11:2276. https://doi.org/10.3390/rs11192276

Li C, Tang L, Ma L, Zhou Y, Gao C, Wang N, Li X, Wang X, Zhu X (2015) Comprehensive calibration and validation site for information remote sensing. Int Arch Photogramm Remote Sens Spatial Inf Sci 40:1233. https://doi.org/10.5194/isprsarchives-XL-7-W3-1233-2015

Li H, He X, Bai Y, Gong F, Li T, Wang D (2024) Intelligent recognition of coastal outfall drainage based on sentinel-2/MSI imagery. Remote Sens 16:423. https://doi.org/10.3390/rs16020423

Li L, Luo H, Zhu H (2014) Estimation of the image interpretability of ZY-3 sensor corrected panchromatic nadir data. Remote Sens 6:4409. https://doi.org/10.3390/rs6054409

Lim P-C, Kim T, Na S-I, Lee K-D, Ahn H-Y, Hong J (2018a) Analysis of UAV image quality using edge analysis. Int Arch Photogramm Remote Sens Spatial Inf Sci 42:359. https://doi.org/10.5194/isprs-archives-XLII-4-359-2018

Lim P-C, Seo J, Kim T (2018b) Extraction of UAV image sharpness index using edge target analysis. Korean J Remote Sens 34:905. https://doi.org/10.7780/kjrs.2018.34.6.1.6

Liu P, Ren C, Wang Z, Jia M, Yu W, Ren H, Xia C (2024) Evaluating the potential of sentinel-2 time series imagery and machine learning for tree species classification in a mountainous forest. Remote Sens 16:293. https://doi.org/10.3390/rs16020293

Mäkiharju SA, Gabillet C, Paik B-G, Chang NA, Perlin M, Ceccio SL (2013) Time-resolved two-dimensional X-ray densitometry of a two-phase flow downstream of a ventilated cavity. Exp Fluids 54:1

Meißner H, Cramer M, Reulke R (2019) Evaluation of structures and methods for resolution determination of remote sensing sensors. Pacific-Rim Symposium on Image and Video Technology. Springer, pp 59–69 https://doi.org/10.1007/978-3-030-39770-8_5

Mhangara P, Mapurisa W, Mudau N (2020) Image interpretability of nSight-1 nanosatellite imagery for remote sensing applications. Aerospace 7:19. https://doi.org/10.3390/aerospace7020019

Mifdal J, Longépé N, Rußwurm M (2021) Towards detecting floating objects on a global scale with learned spatial features using sentinel 2. ISPRS Ann Photogramm Remote Sens Spatial Inf Sci. https://doi.org/10.5194/isprs-annals-V-3-2021-285-2021

NASA A (1973) Advanced scanners and imaging systems for Earth observations. NASA SP-335. Tech. rep., US Govt Printing Office, Washington, DC: NASA

Nguyen LH, Robinson S, Galpern P (2022) Medium-resolution multispectral satellite imagery in precision agriculture: mapping precision canola (Brassica napus L.) yield using Sentinel-2 time series. Precis Agric 23:1051. https://doi.org/10.1007/s11119-022-09874-7

Orych A (2015) Review of methods for determining the spatial resolution of UAV sensors. Int Arch Photogramm Remote Sens Spatial Inf Sci 40:391. https://doi.org/10.5194/isprsarchives-XL-1-W4-391-2015

Pampanoni V, Cenci L, Laneve G, Santella C, Boccia V (2020) On-orbit image sharpness assessment using the edge method: methodological improvements for automatic edge identification and selection from natural targets IGARSS 2020-2020 IEEE International Geoscience and Remote Sensing Symposium. IEEE. https://doi.org/10.1109/IGARSS39084.2020.9324312

Pampanoni V, Cenci L, Laneve G, Santella C, Boccia V (2022) A fully automatic method for on-orbit sharpness assessment: a case study using prisma hyperspectral satellite images IGARSS 2022-2022 IEEE international Geoscience and remote sensing symposium. IEEE. https://doi.org/10.1109/IGARSS46834.2022.9883186

Pampanoni V, Fascetti F, Cenci L, Laneve G, Santella C, Boccia V (2024) Analysing the relationship between spatial resolution, sharpness and signal-to-noise ratio of very high resolution satellite imagery using an automatic edge method. Remote Sens 16:1041. https://doi.org/10.3390/rs16061041

Radoux J, Chomé G, Jacques DC, Waldner F, Bellemans N, Matton N, Lamarche C, d'Andrimont R, Defourny P (2016) Sentinel-2's potential for sub-pixel landscape feature detection. Remote Sens 8:488. https://doi.org/10.3390/rs8060488

Robinson JA, Amsbury DL, Liddle DA, Evans CA (2004) Erratum: Astronaut-acquired orbital photographs as digital data for remote sensing: spatial resolution https://doi.org/10.1080/01431160412331317775

Salamonowicz P (1982) USGS aerial resolution targets. Photogramm Eng Remote Sensing 48:1469

Saleem A, Awange J (2019) Coastline shift analysis in data deficient regions: exploiting the high spatio-temporal resolution sentinel-2 products. CATENA 179:6. https://doi.org/10.1016/j.catena.2019.03.023

Samadzadegan F, Toosi A, Javan FD (2023) Automatic built-up area extraction by feature-level fusion of Luojia 1–01 nighttime light and sentinel satellite imageries in Google Earth Engine. Adv Space Res 72:1052. https://doi.org/10.1016/j.asr.2023.05.015

Schott J, Gerace A, Brown S, Gartley M, Montanaro M, Reuter DC (2012) Simulation of image performance characteristics of the Landsat data continuity mission (LDCM) thermal infrared sensor (TIRS). Remote Sens 4:2477. https://doi.org/10.3390/rs4082477

Scott K, Scott C, Kim HJ, Boyda M (2024) Development of multi-edge slant target for unlocalized MTF measurement of airborne imaging system payloads.

Stankevich SA (2020) Evaluation of the spatial resolution of digital aerospace image by the bidirectional point spread function parameterization International scientific-practical conference. Springer, pp 317–327 https://doi.org/10.1007/978-3-030-58124-4_31

Sun Y, Rao P, Hu T (2021) Parameter design and performance evaluation of a large-swath and high-resolution space camera. Sensors 21:4106. https://doi.org/10.3390/s21124106

Tao Y, Muller J-P (2021) Super-resolution restoration of spaceborne ultra-high-resolution images using the UCL OpTiGAN system. Remote Sens 13:2269. https://doi.org/10.3390/rs13122269

Thomson G (2009) A note on spatial resolution measurement and its implications for image radiometry. Int J Remote Sens 30:1. https://doi.org/10.1080/01431160802339480

Toosi A, Javan FD, Samadzadegan F, Mehravar S, Kurban A, Azadi H (2022) Citrus orchard mapping in Juybar, Iran: analysis of NDVI time series and feature fusion of multi-source satellite imageries. Ecol Inform 70:101733. https://doi.org/10.1016/j.ecoinf.2022.101733

Topan H, Büyüksalih G, Jacobsen K (2005) Information contents of high resolution satellite images EARSel 3D–Remote Sensing Workshop, Porto.

Townshend JR (1981) The spatial resolving power of earth resources satellites. Prog Phys Geogr 5:32

Trujillo-Pino A, Krissian K, Alemán-Flores M, Santana-Cedrés D (2013) Accurate subpixel edge location based on partial area effect. Image Vis Comput 31:72. https://doi.org/10.1016/j.imavis.2012.10.005

Valenzuela AQ, Reyes JCG (2019) Basic spatial resolution metrics for satellite imagers. IEEE Sensors J 19:4914. https://doi.org/10.1109/JSEN.2019.2902512

Valenzuela A, Reinke K, Jones S (2022) A new metric for the assessment of spatial resolution in satellite imagers. Int J Appl Earth Obs Geoinformation 114:103051. https://doi.org/10.1016/j.jag.2022.103051

Wang G, Li Y (1999) Axiomatic approach for quantification of image resolution. IEEE Signal Process Lett 6:257

Wu N, Lv J, Jin W (2024) S4Former: a spectral-spatial sparse selection transformer for multispectral remote sensing scene classification. IEEE Geosci Remote Sens Lett. https://doi.org/10.1109/LGRS.2024.3365509

Xu Y, Zhou J, Zhang Z (2024) A new Bayesian semi-supervised active learning framework for large-scale crop mapping using sentinel-2 imagery. Isprs J Photogramm Remote Sens 209:17. https://doi.org/10.1016/j.isprsjprs.2024.01.023

Zhao L, Shi Y, Liu B, Hovis C, Duan Y, Shi Z (2019) Finer classification of crops by fusing UAV images and Sentinel-2A data. Remote Sens 11:3012. https://doi.org/10.3390/rs11243012